

Diffusion of point defects in crystalline silicon using the kinetic activation-relaxation technique method

Mickaël Trochet,^{1,*} Laurent Karim Béland,^{2,†} Jean-François Joly,^{3,‡} Peter Brommer,^{4,§} and Normand Mousseau^{1,||}

¹*Département de Physique and Regroupement Québécois sur les Matériaux de Pointe (RQMP), Université de Montréal, C.P. 6128, Succursale Centre-Ville, Montréal, Québec, Canada H3C 3J7*

²*Materials Science and Technology Division, Oak Ridge National Laboratory, Oak Ridge, Tennessee 37831-6138, USA*

³*Department of Mechanical and Aerospace Engineering, Carleton University, 1125 Colonel By Drive, Ottawa, Ontario, Canada K1S 5B6*

⁴*Warwick Centre for Predictive Modelling, School of Engineering, and Centre for Scientific Computing,*

University of Warwick, Library Road, Coventry CV4 7AL, UK

(Received 12 March 2015; published 16 June 2015)

We study point-defect diffusion in crystalline silicon using the kinetic activation-relaxation technique (k-ART), an off-lattice kinetic Monte Carlo method with on-the-fly catalog building capabilities based on the activation-relaxation technique (ART nouveau), coupled to the standard Stillinger-Weber potential. We focus more particularly on the evolution of crystalline cells with one to four vacancies and one to four interstitials in order to provide a detailed picture of both the atomistic diffusion mechanisms and overall kinetics. We show formation energies, activation barriers for the ground state of all eight systems, and migration barriers for those systems that diffuse. Additionally, we characterize diffusion paths and special configurations such as dumbbell complex, di-interstitial (IV-pair+2I) superdiffuser, tetrahedral vacancy complex, and more. This study points to an unsuspected dynamical richness even for this apparently simple system that can only be uncovered by exhaustive and systematic approaches such as the kinetic activation-relaxation technique.

DOI: [10.1103/PhysRevB.91.224106](https://doi.org/10.1103/PhysRevB.91.224106)

PACS number(s): 61.72.-y, 05.20.Dd, 05.70.Ln

I. INTRODUCTION

The discovery by Kellogg and Feibelman of the concerted diffusion mechanism for adatom diffusing on a (100) metallic surface, more than 25 years ago, demonstrated the potential richness of atomistic kinetics and the difficulty of predicting these motions through inspection alone [1]. Even for such a simple symmetry, the number of low-energy pathways associated with adatom diffusion turns out to be remarkably large, with concerted diffusion taking place, as discovered later by Henkelman and Jonsson, over a range of atomic distances [2]. Similar complexity is also observed in bulk systems such as silicon [3–7] and iron [8–10], as demonstrated by extensive searches for defect structures and pathways. Understanding these microscopic mechanisms is crucial then for the characterization of long-time defect diffusion and structural evolution.

Finding the relevant self-defect structures and diffusion pathways requires both a reliable physical description and an efficient search and sampling approach. Here, we focus on the latter requirement. Over the years, open-ended search methods such as the activation-relaxation technique (ART nouveau) [11, 12], the dimer, and similar methods [13, 14] have provided useful tools for finding unsuspected pathways to new states. Yet, these search methods do not provide direct kinetic information with respect to these defects.

In this paper, we demonstrate how the use of the kinetic activation-relaxation technique (k-ART), an off-lattice kinetic

Monte Carlo method with on-the-fly catalog building capabilities, can provide detailed characterization of the diffusion pathways of complex defects. To illustrate this, we focus on small self-defect cluster diffusion in bulk Stillinger-Weber crystalline silicon (*c*-Si). This system has received considerable attention over the years [15–17], but a systematic study of defect diffusion is still missing due to the lack of efficient numerical tools. We show that even these simple assemblies, from one to four vacancies and one to four interstitials, can present complex reorganizations that affect considerably their diffusion properties.

This paper is constructed as follows. We first give a brief overview of the kinetic activation-relaxation technique [18, 19]. We then apply k-ART to vacancies and interstitials. Finally, we discuss the relevance of our current results with respect to the general understanding of the diffusion of point defects in crystalline silicon.

II. METHODS: KINETIC ART

All simulations presented here are performed using the kinetic activation-relaxation technique [18, 19]. This algorithm introduces three improvements over standard kinetic Monte Carlo (KMC) [20] in order to treat correctly the kinetics of complex materials.

First, the algorithm is fundamentally off lattice, using a topological classification scheme to identify local environments. This approach makes it possible to handle with the same ease both crystalline and disordered configurations. Second, this topological classification is used to generate an event (see next paragraph) catalog on-the-fly, reducing the amount of computation to be performed at the simulation onset. It also ensures that events associated with new atomic configurations are fully considered. Third, it accounts for

*mickael.laurent.trochet@umontreal.ca

†belandlk@ornl.gov

‡jeanfrancois.joly@carleton.ca

§p.brommer@warwick.ac.uk

||normand.mousseau@umontreal.ca

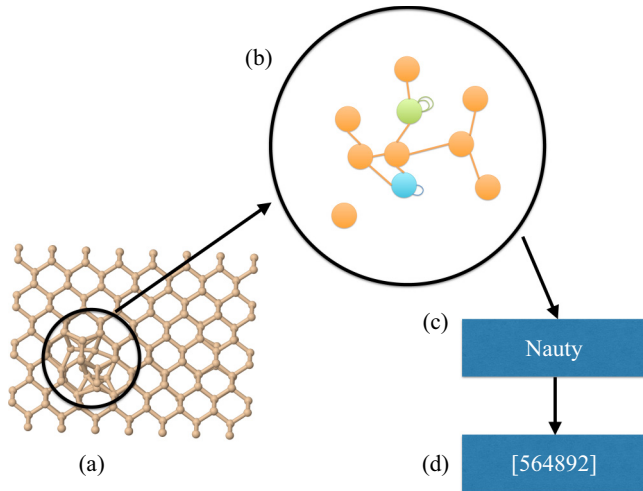


FIG. 1. (Color online) Topological classification using NAUTY. (a) Atoms within a sphere of a given radius around a central atom are extracted from the system. (b) Edges are drawn between pairs of atoms below a cutoff distance. (c) The resulting graph is analyzed by NAUTY and (d) characterized by a unique identifier.

short- and long-range elastic deformations by reconstructing and reconverging all relevant transition-state barriers at every step.

While the k-ART algorithm is described in more details in previous publications [18,19,21–23], we present here a brief description of its implementation.

After a k-ART step, the local topology of each atom is reassessed using the topological analysis package NAUTY [24]. For this, all atoms within a certain radius surrounding an atom (here 6 Å) are selected as vertices of a graph. Edges are drawn between atoms separated by less than a neighbor cutoff (here 2.8 Å). The automorphic group of the resulting graph is then computed, providing a unique identifier and sufficient information to recover permutations and symmetry operations between two automorphic graphs (Fig. 1).

All atomistic environments belonging to the same automorphic group are considered to share a common list of events. After each k-ART move, event searches are launched for all newly identified automorphic groups using ART nouveau, an efficient open-ended transition-state finding algorithm [12,25].

Fifty independent and random searches are launched for each new topology. In order to ensure that events are not missed, new ART nouveau searches are also launched regularly on configurations associated with frequently occurring topologies. In Si, we typically find an average of three to four different events with a barrier below 5 eV per topology. Once the event catalog is updated, events are ordered as a function of their rate, computed using harmonic transition-state theory, as the barriers are high compared to the thermal energy, making them “rare,” with a constant prefactor of 10^{13} Hz. Events within 99.99% of the rate are fully reconstructed and their transition state is relaxed to a precision of 0.02 eV \AA^{-1} , to take into account all elastic and geometric particularities, leading to a energy precision for each specific barrier of 0.01 eV or better. Following standard KMC [26], a time step is computed

according to

$$\Delta t = -\ln(\mu) / \sum_i r_i, \quad (1)$$

where μ is a random number uniformly distributed between 0 and 1 and r_i is the transition rate of event i ; an event is then selected with a probability proportional to its relative weight.

Flickering states, i.e., states of similar energy separated by a relatively low-energy barrier that do not lead to diffusion, are handled using the basin-accelerated mean-rate method (bacMRM) [19] based on the the mean-rate method (MRM) of Puchala *et al.* [27]. As connected flickering states are discovered, they are added into a basin. The basin’s internal kinetics is solved directly and exit rates are corrected for the internal motion. This limits the computational efforts of handling the nondiffusive motion while ensuring a correct kinetics.

A. Topologies versus events

Each atom is associated with a topology based on its surroundings. In a perfect cubic crystal, all atoms have the same environment and, therefore, share the same topology.

If a vacancy is created, a number of new topologies are created, associated with each of the neighboring shell surrounding the vacancy. If the cutoff cluster radius is at the fourth shell, for example, then four new topologies are created attributed to a different number of atoms. Not all topologies, however, correspond to unique and executed events since events, for their part, are attributed to the topology centered on the atom undergoing the largest displacement between the initial and final states.

Still in the case of a single vacancy, the dominant event generated from the three new topologies will be the vacancy first-neighbor diffusion, which will systematically be attributed to the vacancy’s first atomic neighbors allowing us to identify the four new topologies with a single dominant diffusion event.

B. Simulated system

We characterize the diffusion pathways of vacancies and self-interstitials in a crystalline box of 512 Stillinger-Weber Si atoms [28] with periodic boundary conditions. The Stillinger-Weber potential was chosen because this potential ensures the tetrahedron environment of the silicon atoms. It is composed of two terms: a two-body and a three-body term. It is well known that all results extracted from a numerical Monte Carlo simulation are deeply dependent on the potential choice as well as k-ART. For each system, containing between one and four vacancies or interstitials, we perform runs at 500 K. The length of these runs is set as a function of the system’s kinetics and complexity. Vacancies and self-interstitials are created by removing atoms at random position in the box or by adding Si atoms in octahedral sites, respectively. In all cases, the system’s energy is first minimized at $T = 0$ K before k-ART simulations are launched. We compute the formation energy according to

$$E_F = -\left[E_{512} \left(\frac{N}{512} \right) - E \right], \quad (2)$$

TABLE I. Comparison of the formation and migration energies, respectively, E_f and E_m , for the monovacancy obtained by different groups using the Stillinger-Weber potential (SW), tight-binding approximation, and local-density approximation (in eV).

	Vacancy E_f (eV)	E_m (eV)
SW potential		
Our work	2.65	0.51
Gilmer [29]	2.64	0.43
Maroudas [30]	2.66	0.43
Tight-binding approximation		
Lenosky [31]	3.780	
Tang [17]	4.2	0.1
Munro [32]	3.90	0.723
Local-density approximation		
El-Mellouhi [33]	3.36	0.40 ± 0.02

where E_{512} is the total energy of the 512 *c*-Si, N is the number of atoms (from 508 to 516), and E the total energy for the systems studied. We test that this box is large enough to ensure convergence by comparing the configuration energy and activation barriers for the monovacancy and the di-interstitial systems with a 4096-atom box (at constant density), finding a 0.01-eV energy different at most for an overall error on relative energies of at most 0.02 eV.

III. RESULTS

A. Vacancies

1. Monovacancy

At the beginning of each simulation, k-ART performs a local minimization using FIRE that leads to a first metastable configuration. After crossing a low 0.13-eV barrier, the system relaxes a further 1.68 eV to reach the global energy minimum for the monovacancy characterized by a formation energy of $E_{F1V} = 2.65$ eV, in agreement with previous simulations (see Table I). From the relaxed state, k-ART finds one event type with an activation barrier below 5 eV, corresponding to diffusion to the nearest-neighbor crystalline site, with 0.51 eV. It is the only event generated during the 5000-step 500-K simulation samples, corresponding to a 2- μ s simulation time. With displacement of 2.35 Å (distance between two crystalline sites) per jump with the associated time of 13.8 ns, the diffusion coefficient is found to be $D = 4.00 \times 10^{-8} \text{ cm}^2\text{s}^{-1}$. This simulation requires 30 min of CPU time on one 12-core node composed of two processor Intel Westmere-EP X5650 hexa-cores, @2,667GHz.

The barrier we find is slightly higher than that obtained indirectly by Gilmer *et al.* [29] and Maroudas *et al.* [30]. This difference is likely due to the uncertainties on the diffusion coefficient at low temperature used in these two papers to extract the barrier from an Arrhenius plot. Ours is calculated thanks to the mean square displacement versus the simulated time.

2. Divacancy

Divacancy simulations are launched from an initial structure consisting of two isolated vacancies in their fundamental state separated by 11.76 Å. Due to elastic interactions, the two vacancies aggregate rapidly, in less than 30 ns (100 KMC steps), and continue to diffuse as a pair over the next 0.11 s of the 5000-KMC step simulation. The formation energy for the divacancy complex in first-neighbor position is $E_{F2Va} = 4.58$ eV ($E_{F2Va} - 2E_{F1V} = -0.72$ eV), in agreement with literature [34].

Figure 2 shows the energy details for all 5000 accepted events measured with respect to the ground state. Each point represents an executed event which is characterized by an initial-energy state (x axis), a final-energy state (y axis), and an energy barrier (color bar). As an example, the farthest point to the right is associated with the first executed event, at $t = 79.6$ fs, which shows initial and final relative energies of 4.09 and 2.40 eV, respectively, with an energy barrier of 0.14 eV.

Kinetic ART identifies 618 different topologies associated with various configurations for the two vacancies and visits 79 of them during the simulation. Most topologies correspond to the two vacancies approaching and forming a bound complex. Once vacancies reach the ground state, six characteristic configurations dominate, representing more than 95% of all accepted configurations (see top Fig. 3).

These configurations and their associated topologies correspond to vacancies in first- to sixth-nearest-neighbor (NN) position and they are alphabetically named from 2Va to 2Vf. They are connected through 19 different barriers (or events) that control, at 500 K, the divacancy complex diffusion and characterize a surprisingly rich landscape with complex diffusion pathways (see Table II for the details regarding these six states).

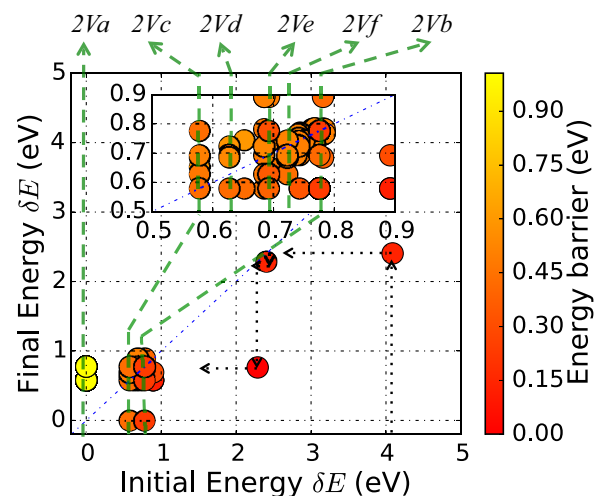


FIG. 2. (Color online) Representation of all 5000 k-ART accepted activation events for the divacancy system (inset: zoom-in between 0.5 to 0.9 eV). All initial and final energies are measured from 2Va, the ground state (set to 0.0 eV). While the x and y axes represent the initial and final energy for each event, the color defines the saddle energy. The energy of the various minima is indicated above the graph and the black arrows represent the trajectory of the first three accepted events.

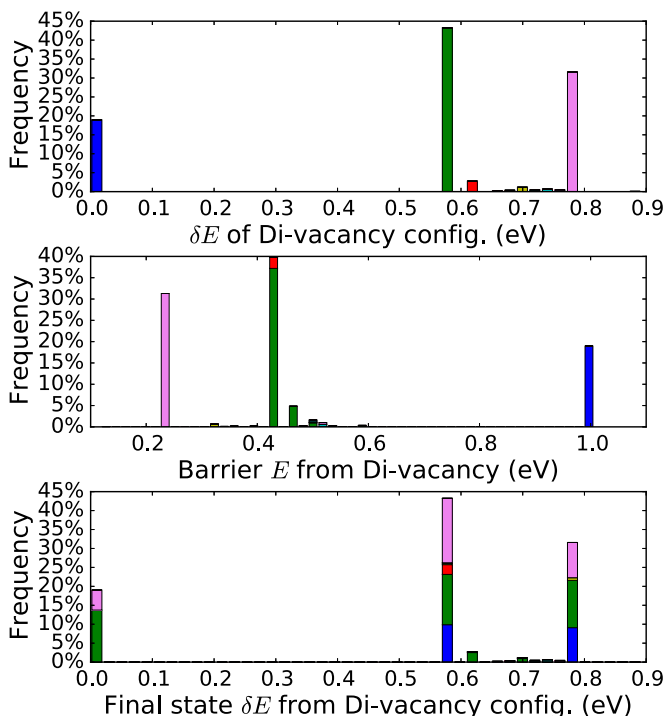


FIG. 3. (Color online) Top panel: Energy histogram of the visited states during the 5000-event simulation of the divacancy with the ground state set at 0.0 eV. Middle panel: Histogram of the activation energy barrier for selected events during the 5000-event simulation. Bottom panel: Energy histogram final state for each of the 5000 accepted events with the ground state set to 0.0 eV. Colors are set according to the energy of initial configurations then used in the two others histograms to follow the possible transition path for each of them. These colors are associated to configurations 2Va (blue), 2Vc (green), 2Vd (red), 2Ve (yellow), 2Vf (cyan), and 2Vb (purple).

Our k-ART simulation reveals two particular features for the divacancy system: First, the 2Vb configuration with the two vacancies in second NN, while crucial for the divacancy complex diffusion, is less stable than the two isolated monovacancy ($E_{F2Vb} - 2E_{F1V} = +0.07$ eV). Second, we observe the presence of a degenerate transition state at 1.00 eV above ground state that connects three states together: the first (2Va), the second (2Vb), and third NN states (2Vc), with relative

TABLE II. Relative configuration energies (ΔE) (top line) and barrier energies for pathways between the six dominant bound states for the divacancy complex. Energies are in eV.

Form	2Va	2Vb	2Vc	2Vd	2Ve	2Vf
ΔE	0	0.78	0.58	0.63	0.68	0.72
2Va		0.235	0.427			
2Vb	1.00		0.432			
2Vc	1.00	0.236		0.521	0.395	
2Vd			0.501		0.478	0.440
2Ve			0.501	0.532		0.489
2Vf				0.532	0.527	

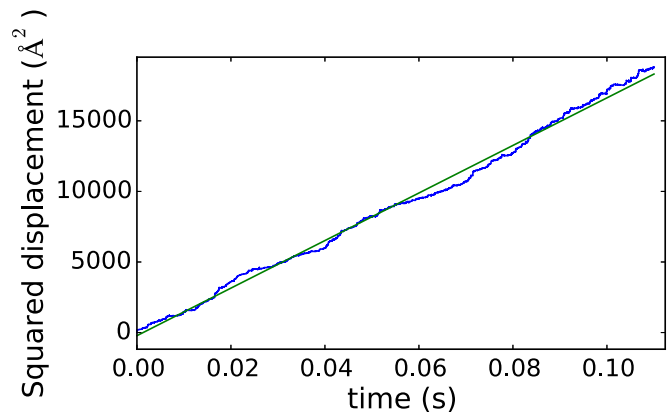


FIG. 4. (Color online) Squared displacement of a function of time (in blue) for the divacancy system. The green line shows a linear regression used to extract the self-diffusion coefficient at 500 K ($D = 1.7 \times 10^{-11}$ cm²s⁻¹).

energies of 0.78 and 0.58 eV, respectively, above ground state (see Fig. 3).

The relatively high energy of 2Vb, with the vacancies in second-neighbor position, is readily explained by bond counting: while most divacancy complexes are associated with only six threefold-coordinated atoms, 2Vb has a seventh one which is twofold coordinated, a very unstable state higher in energy than the eight threefold atoms found with two isolated vacancies.

The previously unknown degenerate saddle point, for its part, was identified straightforwardly by k-ART. It connects three minima through as many pathways (2Va to 2Vb, 2Va to 2Vc, and 2Vb to 2Vc). This leads to a nonuniform diffusion process where the system must first leave the ground state by going through a 1-eV energy barrier, associated with a characteristic time of 50 μ s at 500 K. The system can then diffuse rapidly by repeatedly hopping between 2Vb and 2Vc, with a characteristic time scale of 0.4 ns, determined by the 0.45-eV barrier from 2Vc, before being trapped again in 2Va. These mechanisms dominate the divacancy kinetics although we also observe the two vacancies moving to fourth-, fifth-, and even sixth-neighbor position, before moving back towards the ground state.

Integrating over the 5000 k-ART steps, we find a diffusion coefficient at 500 K of $D = 1.69 \times 10^{-11}$ cm² s⁻¹ corresponding to an average migration barrier of $E_m = 0.84$ eV (see Fig. 4). Clearly, the presence of multiple pathways should also lead to a nonmonotonous thermal behavior as the relative rates for the various mechanisms change as a function of temperature [34].

3. Trivacancy

The trivacancy simulation is launched from an initial structure consisting of three isolated vacancies separated by 10 to 13 Å. It runs for 2000 KMC steps representing 68 ms of simulated time. From the launch of the simulation, the trivacancy complex forms within 58 ms (36 steps), assembling first into a less-mobile divacancy which rapidly attracts the remaining monovacancy. The released energy at these two stages is 6.46 and 0.91 eV, respectively, computed from the

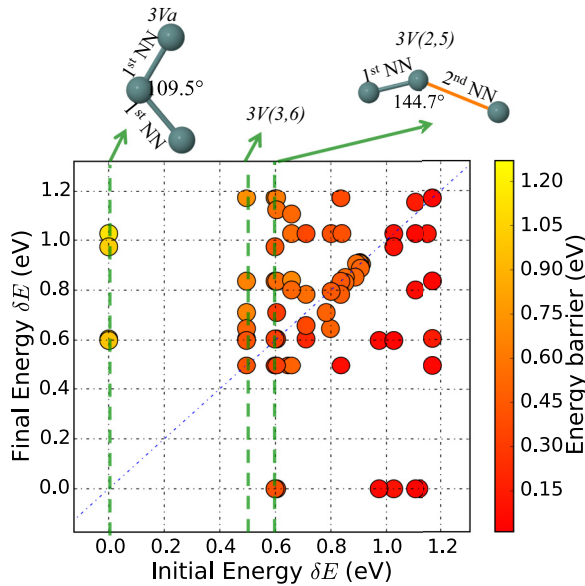


FIG. 5. (Color online) Representation of all 2000 k-ART accepted activation events for the trivacancy system. All initial and final energies are measured from 3Va, the ground state (set to 0). The energy position of the three dominant configurations is indicated. Configurations 3Va and 3V(2,5) are shown above the panel; blue sphere represents empty crystalline silicon site.

three unrelaxed isolated vacancies and the divacancy plus monovacancy relaxed configurations, respectively.

The ground-state formation energy of $E_{F3Va} = 6.41$ eV ($E_{F3Va} - 3E_{F1V} = -1.54$ eV) corresponds to the three vacancies positioned in first-neighbor position on crystalline sites as shown by the 3Va configuration in Fig. 5. Kinetic ART identifies and visits, respectively, 8548 and 514 different topologies associated with various configurations for the three-vacancy system. Once vacancies reach the ground state, three configurations dominate, representing more than 95% of all accepted configurations (see top Fig. 6).

These three configurations are related through seven events that control, at 500 K, the trivacancy complex diffusion, as shown on Fig. 6. These configurations are labeled in the following format: 3V(x,y) (except for the ground state named 3Va), indicating the x th NN and y th NN positions of the monovacancy with respect to the two vacancies of the divacancy complex. With this notation, the jump from one 3V(2,5) to another 3V(2,5) involves the diffusion of one atom from a divacancy complex to an isolated vacancy to form a new divacancy complex. As with 2Vb, we note that the configuration 3V(2,3) is less favorable due to a relative energy of 1.02 eV associated with missing bond, as discussed above.

Although there is a lot of motion, only one actual diffusion event takes place during the k-ART simulation after the trimer is formed. Including various oscillations, it takes place over 100 KMC steps. Neglecting oscillations between various metastable states associated with the 3V(2,5) configuration, it can be reduced, however, to only three steps (see Fig. 7).

Indeed, the 3V(2,5) configuration can reorganize itself at relatively low cost as can be seen in Fig. 8. The 3V(2,5) is connected to two different but equivalent configurations through

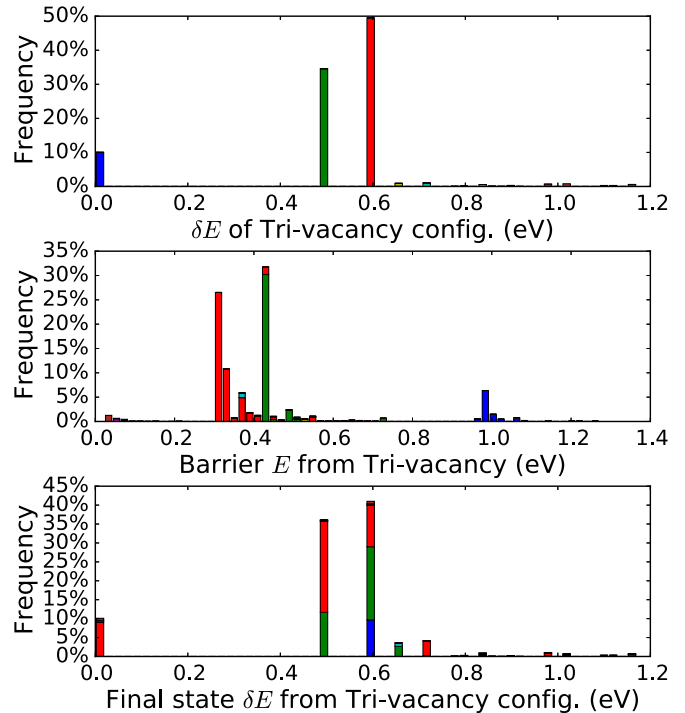


FIG. 6. (Color online) Top panel: Energy histogram of the visited states during the 2000-event simulation of the trivacancy with the ground state set at 0.0 eV. Middle panel: Histogram of the activation energy barrier for selected events during the 2000-event simulation. Bottom panel: Energy histogram final state for each of the 2000 accepted events with the ground state set to 0.0 eV. For the trivacancy system, see Fig. 3 for more information. Configurations 3Va (blue), 3V(3,6) (green), 3V(2,5) (red).

a 0.31-eV barrier that is associated with the reorganization of the divacancy complex, and a third pathway, with a 0.72-eV barrier, that corresponds to an actual diffusion associated with the breaking of the divacancy complex to form a new one (see

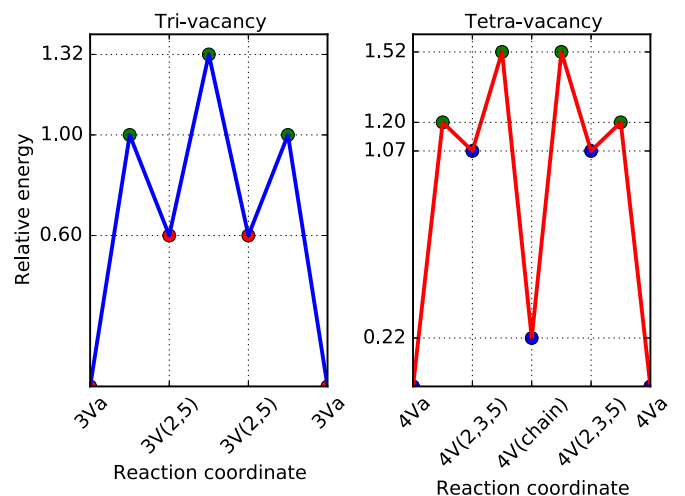


FIG. 7. (Color online) Shortest diffusion mechanisms for the trivacancy (left panel) and the tetravacancy systems (right panel) as measured from the 3Va and 4Va configurations, respectively.

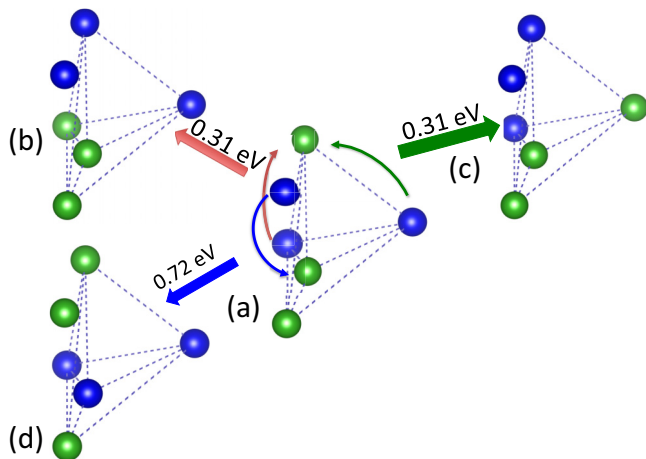


FIG. 8. (Color online) (a)–(d) Cartoon representation of three events connecting different 3V(2,5) configurations. Blue and green color spheres represent silicon atoms and vacancies, respectively. (a) Initial configuration 3V(2,5). (b), (c) Final configuration 3V(2,5) without break of the divacancy. (d) Final configuration 3V(2,5) with break of the divacancy. Red, green, and blue arrows represent movement of silicon atom (thin arrows) and energy barrier (thick arrows) associated to the transition from (a) to (b), (c), and (d), respectively.

Table III for the details regarding these three states energies and activation energies between them).

This shortest three-step diffusion process is the following. First, a jump occurs from the ground state to the configuration 3V(2,5) crossing a 1.00-eV barrier. The diffusive 3V(2,5) to 3V(2,5) move discussed in the previous paragraph (with a 0.72-eV barrier) then takes place followed by the third step, the inverse of the first one, with the vacancy jumping from 3V(2,5) to 3Va with an activation barrier of 0.37 eV:

$$\frac{\tau_{3V,diff}}{\tau_{3V,osc}} = \exp[-(0.72 - 0.31)/k_B T] \approx 7.36 \times 10^{-5}. \quad (3)$$

This three-step diffusion process moves the center of mass of the trivacancy ground state by $\Delta r = 1.97 \text{ \AA}$. The overall limiting migration barrier is $(E_{F3V(2,5)} - E_{F3Va}) + 0.72 \text{ eV} = (0.60 + 0.72) \text{ eV} = 1.32 \text{ eV}$, corresponding to a characteristic time scale of $\Delta t = 2.01 \text{ s}$. The characteristic time scale of $\sim 2 \text{ s}$ explains why it is seen only once in the 68-ms k-ART simulation.

TABLE III. Relative configuration energies (ΔE) (top line) and barrier energies for pathways between the three dominant bound states for the trivacancy complex (nondiffusion motion). The values in parentheses represent a diffusive process. Energies are in eV.

Form		3Va	3V(3,6)	3V(2,5)
To				
ΔE		0	0.496	0.60
3Va				0.37
3V(3,6)			0.42	0.31
3V(2,5)		1.00	0.42	0.31 (0.72)

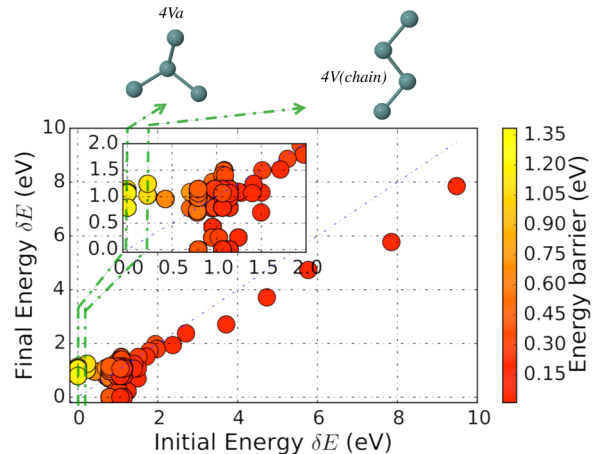


FIG. 9. (Color online) Representation of all 2671 k-ART accepted activation events for the tetravacancy system. All initial and final energies are measured from 4Va, the ground state (set to 0). Inset: zoom-in between 0 and 2 eV. Configurations 4Va and 4V(chain) are shown above the figure.

4. Tetravacancy

Tetravacancy simulations are launched from an initial structure consisting of four isolated vacancies positioned from 3.8 to 7.7 \AA apart and run for 2671 KMC steps, representing 7.29 s of simulation time. From the initial configuration, the tetravacancy forms within 2.50 ms (155 steps), faster than for the three-vacancy system due to the increased defect density. With a formation energy of $E_{F4Va} = 7.93 \text{ eV}$ ($E_{F4Va} - 4E_{F1V} = -2.67 \text{ eV}$), the ground state corresponds to a four-vacancies truncated tetrahedron (see configuration 4Va in Fig. 9).

K-ART identifies and visits 12360 and 1010 different topologies associated with various configurations for the three-vacancy system, respectively. Once vacancies reach the ground state, seven configurations dominate the dynamic of the system, representing more than 90% of all accepted configurations (see top Fig. 10).

These configurations are related through 27 different events that control, at 500 K, the tetravacancy complex diffusion (see Table IV). As indicated, the barrier for leaving the ground state is fairly high, at 1.2 eV, associated with a 0.13-s time scale. The nearest excited states correspond to a monovacancy hovering around the trivacancy remaining cluster since further splitting of the trivacancy cluster requires crossing an additional 1.0 eV barrier. We therefore identify the various topologies around the ground state as 4V(x, y, z) with x, y , and z corresponding to the monovacancy position, in units of neighbor shell, with respect to the the trivacancy complex. Once again, dangling bond distribution provides a qualitative explanation for the relative energies of the various states.

Because the cost associated with splitting the tetravacancy into a divacancy plus either two monovacancies or a divacancy complex is of the order of 2.2 eV or more, the tetravacancy cluster diffuses through a dominant four-step mechanism that preserves a compact trivacancy complex at all times. In its simplest implementation, as shown in Fig. 7(b), a monovacancy first moves to second-neighbor position by crossing a 1.2-eV barrier [originating 4Va and reaching 4V(2,3,5)]. After another

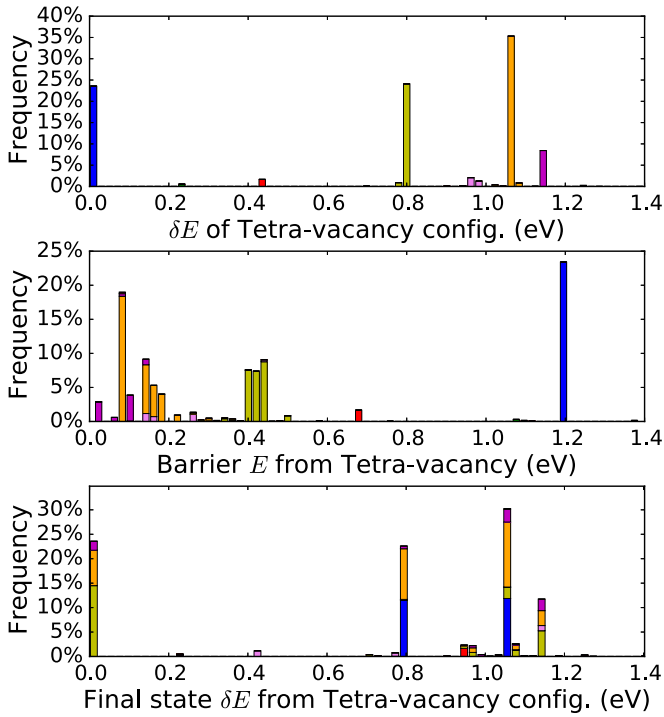


FIG. 10. (Color online) Top panel: Energy histogram of the visited states during the 2671-event simulation of the tetravacancy with the ground state set at 0.0 eV. Middle panel: Histogram of the activation energy barrier for selected events during the 2671-event simulation. Bottom panel: Energy histogram final state for each of the 2671 accepted events with the ground state set to 0.0 eV. For the tetravacancy system (see Fig. 3 for more information). Configurations 4Va (blue), 4V(chain) (green), 4V(3,4,6) (yellow), 4V(6,7,11) (pink), 4V(2,3,5) (orange), 4V(2,3,5)* (purple).

jump of 0.45 eV, the tetravacancy cluster adopts a compact chainlike conformation, only 0.22 eV above the ground state [originating from 4V(2,3,5) and reaching 4V(chain)]. From this state, the system diffuses by moving the vacancy at the other end of the chain, through a two-step motion, into the compact truncated tetrahedron state, with a displacement of $\Delta r = 1.50 \text{ \AA}$.

This diffusion pathways require crossing barriers totaling 1.52 eV with a characteristic time scale, at 500 K, of 209 s,

TABLE IV. Relative configuration energies (ΔE) (top line) and barrier energies for pathways between the seven dominant bound states for the tetravacancy complex. The values in parentheses represent alternative higher saddle points and starred values are transition found in catalog but not executed during the simulation. Energies in eV.

Form	4Va	4V(3,4,6)	4V(6,7,11)	4V(2,3,5)	4V(2,3,5)*	4V(chain)	4V(2,5,8)
ΔE	0	0.79	0.97	1.07	1.14	0.22	1.24
4Va		0.41		0.13	0.06		
4V(3,4,6)	1.20		0.31	0.16	0.1		
4V(6,7,11)		0.49		0.22	0.14 and 0.27		
4V(2,3,5)	1.20	0.44	0.32	0.04 and 0.17	0.24	1.30	
4V(2,3,5)*	1.20	0.44	0.31 and 0.44	0.17	0.1		
4V(chain)				0.45			0.09
4V(2,5,8)						1.10	

well beyond the reach of any standard simulation method. Yet, it was identified and generated without bias with k-ART.

Altogether, the diffusing behavior of growing vacancy clusters shows a clear critical slowing down; these act as traps that become more and more effective with cluster size in the absence of collective mechanism that could overcome this trend. The situation, as we will see, is different with interstitials.

B. Interstitials

1. Monointerstitial

A monointerstitial simulation is launched from an initial structure consisting of one isolated adatom placed in an octahedral site of the silicon crystal, and run for 5797 KMC steps, representing 1.58 ms of simulation time. After minimization on the first KMC step, the ground state is reached with a formation energy of $E_{F11a} = 3.685 \text{ eV}$ ($E_{F11a} = 1.035 \text{ eV}$ vs E_{F1V}). It represents a monointerstitial dumbbell complex (1Ia) with the silicon adatom and a neighbor *c*-Si atom sharing the crystalline site (by displacement of the *c*-Si atom from its crystalline site).

K-ART identifies 3929 different topologies and visits 204 of them during the simulation. Most are associated with the interstitial in various dumbbell configurations. In spite of these large numbers, the dynamics is dominated by two configurations that represent more than 95% of all accepted configurations.

Figure 11 shows three mechanisms named A, B, and C that control, at 500 K, the monointerstitial complex diffusion. Remarkably, each of these mechanisms is associated with the same two different saddle points as indicated in the figure. For example, mechanism A is a one-step process connecting two ground-state configurations. This diffusion can take place either through saddle 1, at 0.78 eV above ground state, or saddle 2, at 0.94 eV. Mechanism B connects the two 1Ib configurations (the metastable state at 0.75 eV above the ground state through the *same* barriers). Finally, mechanism C is a multiple-diffusion-steps process that inserts the B mechanism into the A one. C' shortest pathway is a jump from 1Ia to 1Ib going down to 1Ia with, at all steps, the possibility to pass through the low or the high saddle point.

Previous work had shown a migration barrier of 0.9 [29] and 0.77 eV [35] using MD simulations, but not identifying the degeneracy clearly observed here. K-ART is able to find two

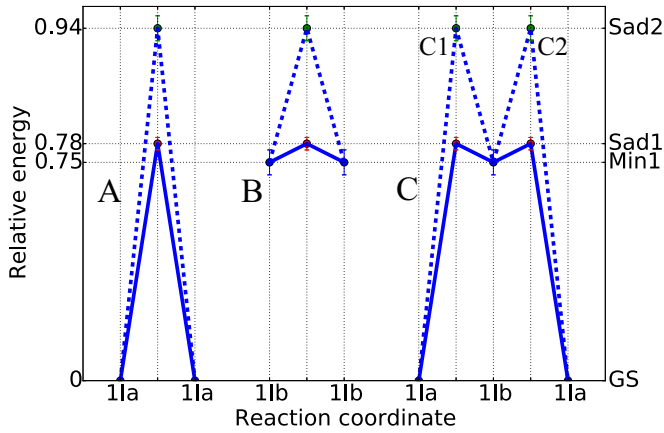


FIG. 11. (Color online) Diffusion mechanisms for the mono-interstitial. Lines represent events passing by the low saddle point (Sad1), dot lines represent events passing by the high saddle point (Sad2). Mechanisms denote A, B, and C are events, from and to the ground state 11a, from and to the metastable state 11b, and from 11a to 11a passing by 11b, respectively. C1, C2 correspond to transition from 11a to 11b, from 11b to 11a, respectively.

events with same initial and final configurations but passing by two different saddle points. These events are associated with the symmetric transition 11a with activation energies of 0.78 or 0.94 eV according to the saddle point chosen. The difference in activation energies of these transition is due to the elasticity of surrounding *c*-Si atoms that allow different transition path. As expected, the probability of passing by the low (high) saddle point is 97%(3%), respectively, as expected according to the ratio of the transition rate of both events at 500 K:

$$\frac{\tau_{11a-sad2-11b}}{\tau_{11a-sad1-11b}} = \exp[-(0.94 - 0.78)/k_B T] \approx 0.03. \quad (4)$$

Mechanism A (or C1) passing by the low saddle point of 0.78 eV, associated to a 7.26- μ s time scale is the limiting activation energy that allows the complex to diffuse. The diffusion mechanism is characterized by a displacement of 3.84 Å since it is a diffusion process in second-nearest-neighbor jump.

2. Di-interstitials

A di-interstitial simulation is launched from an initial structure consisting of two isolated adatoms separated by 9 Å. The simulation is run for 1048 KMC steps for a total of 128 μ s.

Aggregation into the ground state occurs over 28 KMC steps and takes most of the 128 μ s, with a formation energy of $E_{F21a} = 5.74$ eV ($E_{F21a} - 2E_{F11a} = -1.63$ eV) for the two adatoms in first-neighbor position. This structure involves a local reconstruction of the network that corresponds to the combination of two interstitials with 2 IV pairs or two dumbbells back to back and is denoted 21a.

This 21a structure kinetics is dominated by a 0.28-eV two-step one-dimensional diffusion mechanism that takes place along the 110 axis. Indeed, while k-ART identifies and visits, respectively, 9378 and 458 different topologies associated with various configurations for the two adatoms (see Fig. 12 and top Fig. 13), the 21a and its associated excited state 21b, shown in Fig. 12, represent more than 95% of all accepted events. This

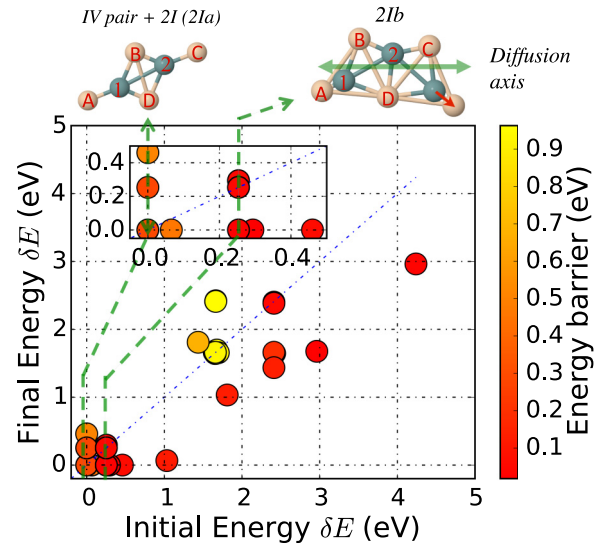


FIG. 12. (Color online) Representation of all 1048 k-ART accepted activation events for the di-interstitial system. All initial and final energies are measured from 21a, the ground state (set to 0). Inset: zoom-in of the region 0 to 0.5 eV. The ground state 21a and metastable state 21b are represented above the panel. Blue and beige spheres represent empty crystalline site and off-lattice Si atoms, respectively.

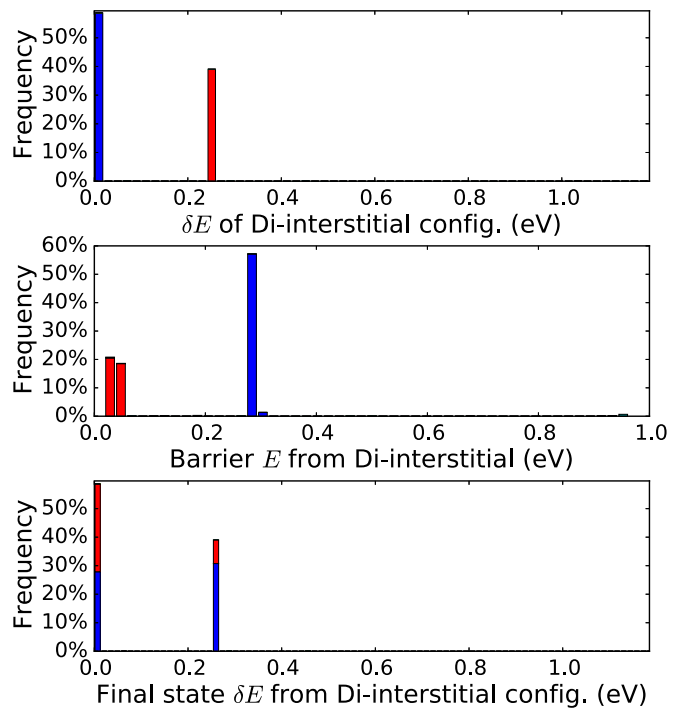


FIG. 13. (Color online) Top panel: Energy histogram of the visited states during the 1048-event simulation with the ground state set at 0.0 eV. Middle panel: Histogram of the activation energy barrier for selected events during the 1048-event simulation. Bottom panel: Energy histogram final state for each of the 1048 accepted events with the ground state set to 0.0 eV. For the di-interstitial system (see Fig. 3 for more information). Configurations 21a (blue), 21b (red).

excited state, with an energy of only 0.03 eV below the barrier, can be seen as the center of a long energy plateau between two 2Ia states.

The top of Fig. 13 clearly shows two configurations that lead to four different events controlling the 2Ia complex diffusion at 500 K. These events are transitions 2Ia to 2Ib, 2Ib to 2Ia, symmetric 2Ia, and symmetric 2Ib.

Diffusion of the di-interstitial complex is essentially one dimensional. The effective migration energy is found to be 0.28 eV with a basic jump $\Delta x = 1.92 \text{ \AA}$.

This result is in agreement with Gilmer *et al.* [29] who had observed a 0.2-eV migration barrier for the di-interstitial without providing a description. The very low-energy barrier of this complex, half that of the vacancy, makes it the fastest self-defect diffuser in silicon.

3. Tri-interstitials

The tri-interstitial simulation is launched from an initial structure consisting of three isolated adatoms separated by 3 to 10 Å. It runs for 13 623 KMC steps, representing 22.54 s of simulated time (see Fig. 14). From the initial configuration, the tri-interstitial ground state is formed within 58 ms, corresponding to 5028 steps due to the high activation barrier associated with interstitial migration.

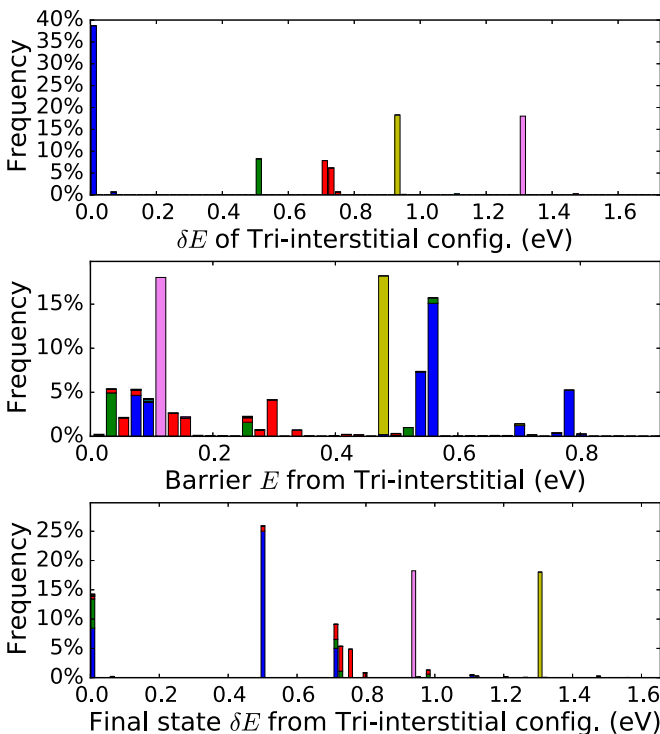


FIG. 14. (Color online) Top panel: Energy histogram of the visited states during the 13 623-event simulation with the ground state set at 0.0 eV. Middle panel: Histogram of the activation energy barrier for selected events during the 13 623-event simulation. Bottom panel: Energy histogram final state for each of the 13 623 accepted events with the ground state set to 0.0 eV. For the tri-interstitial system (see Fig. 3 for more information). Configurations 3Ia (blue), 3Ib (green), 3Ic (red), 3Id (yellow), 3Ie (pink).

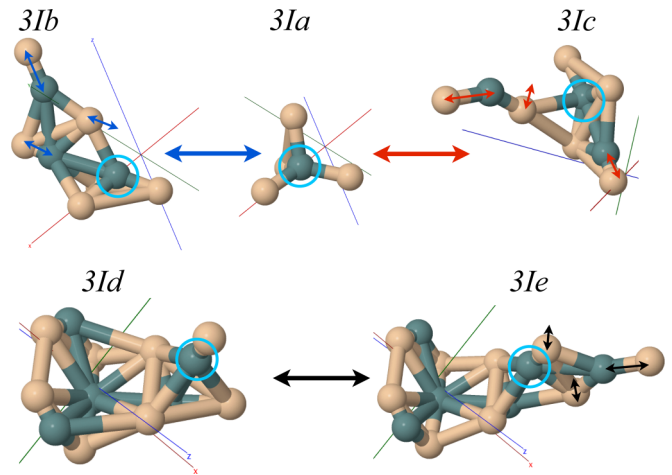


FIG. 15. (Color online) Dominant configurations and transitions for the tri-interstitial system. Si atoms are in beige color and empty crystalline sites are in blue. A cyan circle is used as a reference point for the configurational changes. Arrows show movement of atoms (thin arrow) over structural transitions (thick arrow).

The ground state has a formation energy of $E_{F3I} = 7.21 \text{ eV}$ ($E_{F3Ia} - 3E_{F1Ia} = -3.85 \text{ eV}$) and corresponds to a tetrahedral complex composed of four atoms out of crystalline site around a commonly shared crystalline site (Fig. 15).

Kinetic ART identifies 102 543 different topologies associated with various configurations for the three adatoms and visits 2062 of them. Once the three adatoms aggregate, five configurations associated with the bound tri-interstitial are found to dominate, representing more than 95% of all accepted configurations (Fig. 16). Indeed, once the tri-interstitial complex is formed, it is trapped for the whole 22.54 s of simulation, with the atoms exploring four nearby bound states represented in Fig. 15.

As shown in Fig. 15, the three-interstitial ground state 3Ia can be seen as four Si atoms sharing a crystalline site forming a tetrahedron around it. From this point, the complex can explore the locally bound states by moving one interstitial at a time to a neighbor state. However, the elastic deformation is large

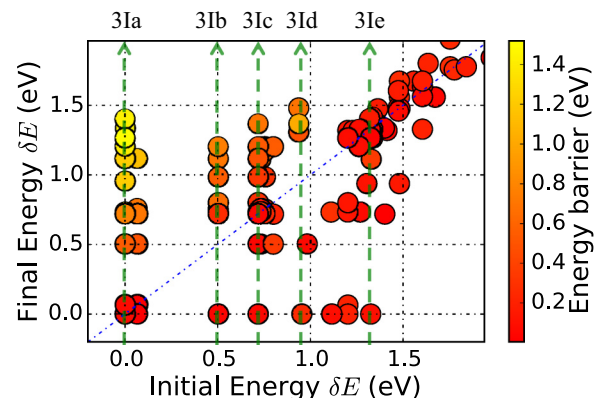


FIG. 16. (Color online) Representation of all 13 623 k-ART accepted activation events for the tri-interstitial system. All initial and final energies are measured from 3Va, the ground state (set to 0). Relative energies for the various states are indicated.

TABLE V. Relative minimum (ΔE) (top line) and barrier energies for pathways between the five dominant bound states for the tri-interstitial complex. The values in parentheses represent alternative higher saddle points and starred values are transition found in the catalog but not executed during the simulation. Energies are in eV.

Form		3Ia	3Ib	3Ic	3Id	3Ie
To						
ΔE		0	0.50	0.72	0.94	1.31
3Ia		0.07	0.05 (0.20*)	0.06		
3Ib		0.55 (0.70)		0.02 (0.28)		
3Ic		0.78	0.24 (0.50)	0.04		0.35
3Id						0.11
3Ie				0.94*	0.49	

enough to prevent the breakup of the complex, even on the extended simulated time scale reached here. The first 5000 events consist mostly of an oscillation 3Id and 3Ie states, with a forward and reverse energy barrier of 0.49 and 0.11 eV, respectively (Table V).

This oscillation is broken by a transition from 3Ie to 3Ic associated with an energy barrier of 0.35 eV, 0.24 eV higher than that associated in the 3Ie to 3Id states oscillation. At 500 K, this pathway with respect to the oscillation is 0.3%. From 3Ic, the system moves rapidly into the ground state, 0.94 eV below 3Id, and remains trapped for the rest of the simulation.

The lowest pathway for the tri-interstitial diffusion requires crossing a total barrier of 1.66 eV, associated with a 5544-s (1.54-h) time scale. No diffusion from the ground state is observed in our 22.54-s simulation.

4. Tetrainterstitials

The tetrainterstitial simulation is launched from an initial structure consisting of four isolated adatoms separated by 6.0 to 9.6 Å. It is run for 1595 KMC steps reaching 13.53 μ s of simulation time. From the initial configuration, the tetrainterstitial forms within 10.7 ns, after 26 KMC steps.

We find a formation energy of $E_{F4Ia} = 9.35$ eV ($E_{F4Ia} - 4E_{F1Ia} = -5.39$ eV) for the ground state (see 4Ia in Fig. 17). During the simulation, k-ART identifies 85 412 different topologies and visits 2685 of them. As for the other complexes, however, only a small number of bound states dominate (five here), representing more than 85% of all accepted configurations (see Fig. 17 and top Fig. 18).

The two lowest-energy states are shown in inset in Fig. 17. 4Ia corresponds as a chainlike complex composed of five atoms around the center crystalline site and two other atoms pushed away from their crystalline position. The most visited configuration is the complex 4Ib with an energy is 0.15 eV above 4Ia and a minimum energy barrier of 0.48 eV between the two states (see Table VI for the details regarding these five states energies and activation energies between them).

Interestingly, and contrary to the tri-interstitial, the tetrainterstitial complex diffuses relatively rapidly as a bound state. Figure 19 shows a diffusion mechanism for the tetrainterstitial system. From the ground state 4Ia, the system reaches the configuration 4Ib by crossing an activation energy of

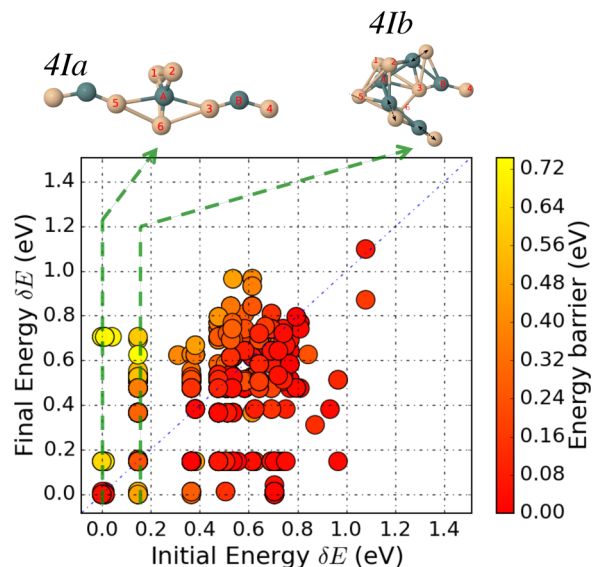


FIG. 17. (Color online) Representation of all 1595 k-ART accepted activation events for the tetrainterstitial system. The ground state 4Ia and configuration 4Ib are shown above the panel. All initial and final energies are measured from 4Ia, the ground state (set to 0).

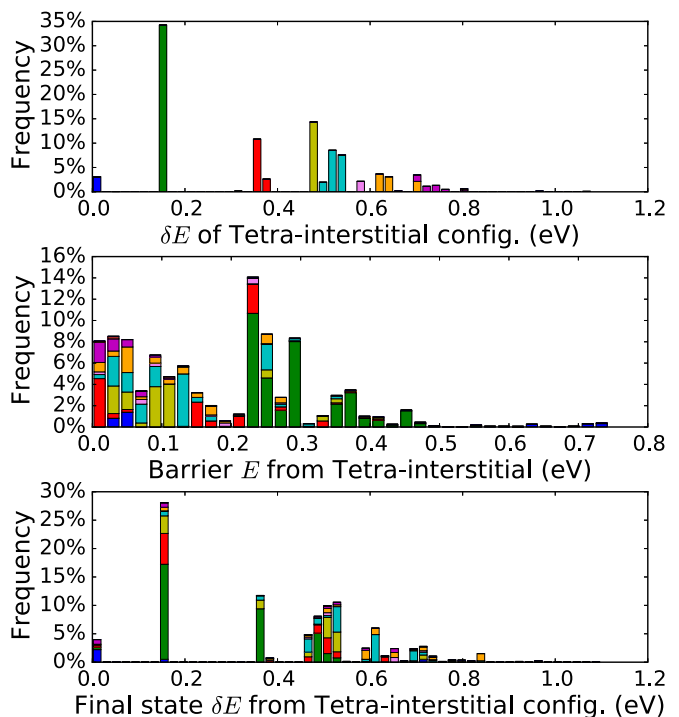


FIG. 18. (Color online) Top panel: Energy histogram of the visited states during the 1595-event simulation with the ground state set at 0.0 eV. Middle panel: Histogram of the activation energy barrier for selected events during the 1595-event simulation. Bottom panel: Energy histogram final state for each of the 1595 accepted events with the ground state set to 0.0 eV. For the tetrainterstitial system (see Fig. 3 for more information). Configurations 4Ia (blue), 4Ib (green), class 4Ic (red), configuration 4Id (yellow), class 4Ie (cyan).

TABLE VI. Relative configuration energies (ΔE) (top line) and barrier energies for pathways between the five dominant bound states for the tetrainterstitial complex. Values in parentheses represent alternative higher saddle points and starred values are transition found in catalog but not executed during the simulation. Energies are in eV.

Form	4Ia	4Ib	4Ic	4Id	4Ie
ΔE	0	0.148	0.36–0.38	0.48	0.50–0.53
4Ia	0.04	0.48	0.28	0.14	
4Ib	0.63 (0.69; 0.73)	0.23	0.01; 0.17*	0.03	0.18
4Ic	0.65*	0.23; 0.39*	0.03	0.03	0.06
4Id		0.36	0.15	0.10	0.05
4Ie		0.56	0.22	0.10	0.02 (0.57)

0.63 eV. From the configuration 4Ib the system reaches the configuration 4Ie by crossing a barrier with an activation energy of 0.56 eV, then, a transition from 4Ie to 4Ia with an activation energy of 0.57 eV. From here, the complex diffused and goes back to the ground state 4Ia. This complex diffusion mechanism leads to a simple atomic jump with $\Delta r = 2.35 \text{ \AA}$ with a limiting migration energy of $E_m = 1.10 \text{ eV}$, associated to a 12.2-ms time scale.

IV. DISCUSSION AND CONCLUSION

We have explored the energy landscape associated with a small number of self-defects in *c*-Si, demonstrating a surprising richness for such simple systems. Characterization of this richness is made possible with the use of an unbiased off-lattice accelerated method, kinetic ART, an off-lattice kinetic Monte Carlo algorithm with on-the-fly catalog building capabilities. (Kinetic ART is still under development, but a version is available for distribution. To receive the code or for more information, please see the Supplemental Material [36].) In this paper, we focus more precisely on the aggregation and diffusion processes associated with vacancies and interstitials in *c*-Si described with the Stillinger-Weber potential [28]. We characterize the nature and kinetics of several self-defect complexes, some already known, most of them newly described.

With kinetic ART, we recover the basic diffusion barriers already identified in previous numerical work [17,29–35], such

as the monovacancy and monointerstitial migration barriers. The number of possible barriers, however, is found to be much larger than what had previously been found, with those relevant at 500 K multiplying the complexity of the system. We find, for example, that degenerate or quasidegenerate saddle points are not so rare, contrary to what is normally thought. These states play an important role in the divacancy and the monointerstitial diffusion. We also show that, while vacancy clusters become less and less mobile as they grow, the mobility associated with interstitial clusters is not monotonous with size: while the monointerstitial and tri-interstitial are pinned by very high-energy barriers, the di-interstitial can reconstruct as a raft with a diffusion barrier lower than that of the monovacancy and the tetrainterstitial can move around by moving a single atom around a tri-interstitial cluster, accelerating considerably its diffusion. This forces us to revise our general understanding of self-diffusion and, very likely, diffusion in general as we find that local defects can undergo considerable geometric reconstruction that modifies their diffusion properties.

If the general application of the specific results presented here is limited by the use of an empirical potential, the general findings raise the possibility of complex diffusion mechanisms even in systems as simple as the one presented here. Recovering dominant diffusion, but also trapping mechanisms, requires clearly well beyond the identification of a few configurations by symmetry analysis or through molecular dynamics that cannot offer a detailed characterization for temperatures well below melting, particularly because some of the transformations require visiting metastable states that cannot survive these high temperatures and can only play a dynamical and structural role at lower temperature.

The development of accelerated methods such as kinetic ART opens up a whole new area of study into mechanisms that we did not know existed until now. The systematic use of such methods will help improve considerably our understanding of diffusion at the atomistic level in materials.

ACKNOWLEDGMENTS

This work has been supported by the Canada Research Chairs program and by grants from the Natural Sciences and Engineering Research Council of Canada (NSERC) and the Fonds Québécois de la Recherche sur la Nature et les Technologies (FQRNT). We are grateful to Calcul Québec for generous allocations of computer resources.

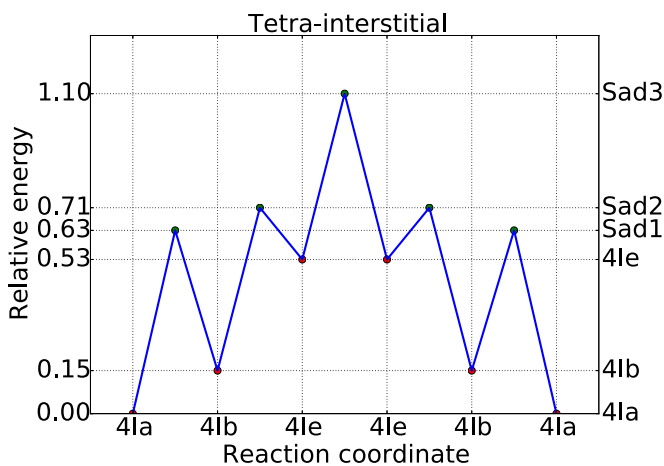


FIG. 19. (Color online) Shortest diffusion mechanisms for the tetrainterstitial system. (The 0 eV is 4Ia configuration for the tetravacancy.)

- [1] G. L. Kellogg and P. J. Feibelman, *Phys. Rev. Lett.* **64**, 3143 (1990).
- [2] G. Henkelman and H. Jonsson, *J. Chem. Phys.* **115**, 9657 (2001).
- [3] Y. a. Du, R. G. Hennig, T. J. Lenosky, and J. W. Wilkins, *Eur. Phys. J. B* **57**, 229 (2007).
- [4] H. Park and J. W. Wilkins, *Appl. Phys. Lett.* **98**, 171915 (2011).
- [5] N. E. B. Cowern, S. Simdyankin, C. Ahn, N. S. Bennett, J. P. Goss, J.-M. Hartmann, A. Pakfar, S. Hamm, J. Valentin, E. Napolitani, D. De Salvador, E. Bruno, and S. Mirabella, *Phys. Rev. Lett.* **110**, 155501 (2013).
- [6] H. Kallel, N. Mousseau, and F. Schiettekatte, *Phys. Rev. Lett.* **105**, 045503 (2010).
- [7] L. K. Béland, Y. Anahory, D. Smeets, M. Guihard, P. Brommer, J.-F. Joly, J.-C. Pothier, L. J. Lewis, N. Mousseau, and F. Schiettekatte, *Phys. Rev. Lett.* **111**, 105502 (2013).
- [8] M.-C. Marinica, F. Willaime, and N. Mousseau, *Phys. Rev. B* **83**, 094119 (2011).
- [9] M.-C. Marinica, F. Willaime, and J.-P. Crocombette, *Phys. Rev. Lett.* **108**, 025501 (2012).
- [10] P. Brommer, L. K. Béland, J.-F. Joly, and N. Mousseau, *Phys. Rev. B* **90**, 134109 (2014).
- [11] G. T. Barkema and N. Mousseau, *Phys. Rev. Lett.* **77**, 4358 (1996).
- [12] R. Malek and N. Mousseau, *Phys. Rev. E* **62**, 7723 (2000).
- [13] D. Wales and J. Doye, *J. Phys. Chem. A* **101**, 5111 (1997).
- [14] G. Henkelman and H. Jónsson, *J. Chem. Phys.* **111**, 7010 (1999).
- [15] G. A. Baraff and M. Schlüter, *Phys. Rev. B* **30**, 3460 (1984).
- [16] Y. Bar-Yam and J. D. Joannopoulos, *Phys. Rev. Lett.* **52**, 1129 (1984).
- [17] M. Tang, L. Colombo, J. Zhu, and T. Diaz de la Rubia, *Phys. Rev. B* **55**, 14279 (1997).
- [18] F. El-Mellouhi, N. Mousseau, and L. J. Lewis, *Phys. Rev. B* **78**, 153202 (2008).
- [19] L. K. Béland, P. Brommer, F. El-Mellouhi, J.-F. Joly, and N. Mousseau, *Phys. Rev. E* **84**, 046704 (2011).
- [20] A. F. Voter, *Radiation Effects in Solids*, NATO Science Series (Springer, Berlin, 2007), pp. 1–23.
- [21] J.-F. Joly, L. K. Béland, P. Brommer, F. El-Mellouhi, and N. Mousseau, *J. Phys.: Conf. Ser.* **341**, 012007 (2012).
- [22] N. Mousseau, L. K. Béland, P. Brommer, J.-F. Joly, F. El-Mellouhi, E. Machado-Charry, M.-C. Marinica, and P. Pochet, *J. At., Mol. Opt. Phys.* **2012**, 1 (2012).
- [23] N. Mousseau, L. K. Béland, P. Brommer, F. El-Mellouhi, J.-F. Joly, G. K. N'Tsouaglo, O. Restrepo, and M. Trochet, *Comput. Mater. Sci.* **100**, 111 (2015).
- [24] B. D. McKay, *Congr. Numer.* **30**, 45 (1981).
- [25] E. Machado-Charry, L. K. Béland, D. Caliste, L. Genovese, T. Deutsch, N. Mousseau, and P. Pochet, *J. Chem. Phys.* **135**, 034102 (2011).
- [26] A. Bortz, M. Kalos, and J. Lebowitz, *J. Comput. Phys.* **17**, 10 (1975).
- [27] B. Puchala, M. L. Falk, and K. Garikipati, *J. Chem. Phys.* **132**, 134104 (2010).
- [28] F. H. Stillinger and T. A. Weber, *Phys. Rev. B* **31**, 5262 (1985).
- [29] G. Gilmer, T. Diaz de la Rubia, D. Stock, and M. Jaraiz, *Nucl. Instrum. Methods, Phys. Res. Sect. B* **102**, 247 (1995).
- [30] P. E. Parris and B. D. Bookout, *Phys. Rev. B* **47**, 15562 (1993).
- [31] T. J. Lenosky, J. D. Kress, I. Kwon, A. F. Voter, B. Edwards, D. F. Richards, S. Yang, and J. B. Adams, *Phys. Rev. B* **55**, 1528 (1997).
- [32] L. J. Munro and D. J. Wales, *Phys. Rev. B* **59**, 3969 (1999).
- [33] F. El-Mellouhi, N. Mousseau, and P. Ordejón, *Phys. Rev. B* **70**, 205202 (2004).
- [34] D. Caliste and P. Pochet, *Phys. Rev. Lett.* **97**, 135901 (2006).
- [35] L. A. Marqués, L. Pelaz, P. Castrillo, and J. Barbolla, *Phys. Rev. B* **71**, 085204 (2005).
- [36] See Supplemental Material at <http://link.aps.org/supplemental/10.1103/PhysRevB.91.224106> for eight files containing atomic positions for various defect configurations in *xyz* format and a text file describing the arrangement of frames in each *xyz* file.